
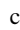
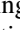


Finite wing lift during water-to-air transition

W. A. Weisler , R. Waghela,^{*} K. Granlund , and M. Bryant [†]*Mechanical and Aerospace Engineering, North Carolina State University, 911 Oval Drive, Raleigh, North Carolina 27695, USA*

(Received 24 October 2019; accepted 8 March 2021; published 12 May 2021)

Wings are used for numerous applications in both air and water and their lift generation in either domain is well understood. However, the lift generated by a wing when it is transitioning out of water and into air has not been quantified to date. This experimental study aims to examine the lift generated by a wing as it performs this water egress. An aspect ratio 4, NACA 0015 wing is translated at constant velocity to investigate the effects of starting depth under the surface, angle of attack, and egress velocity. For all test cases, the wing is translated at constant velocity for at least two chords prior to piercing the surface and the lift profile during the egress is similar for all tested starting depths. The angle of attack affects the time-dependent lift after start and the distance traveled to achieve steady state due to flow attachment changes. However, the angle of attack was not observed to affect the lift profile during egress. The lift history is strongly dependent on egress velocity. Lower velocities register a large lift overshoot followed by a negative lift undershoot before the egress is complete. Higher velocities do not exhibit either overshoot or undershoot and exhibit a more linear transition profile.

DOI: [10.1103/PhysRevFluids.6.054002](https://doi.org/10.1103/PhysRevFluids.6.054002)

I. INTRODUCTION

The concept of a vehicle capable of both flight and underwater operations has been of interest as far back as the 1930s [1]. Only recently have proof-of-concept vehicles capable of freely transitioning and operating in both the aerial and underwater domains been demonstrated [1–5]. This class of cross-domain vehicles enables a myriad of civilian and military capabilities. As design of these vehicles continues, improved understanding of the relevant flow physics is needed. While the understanding of fluid dynamics for airplanes and submersibles is well established, the transition between these domains is not well understood and is currently being investigated. Previous works have investigated efficient propulsion methods for these domains [6] and dynamic modeling of passively draining structures for cross-domain vehicles [7]. However, for maintaining control of a vehicle, an important missing element of this transition is an understanding of the changes in wing lift during egress.

Existing studies of the water-air interface transition have been mostly motivated by naval and industrial needs such as ship hulls entering and exiting the water in large swells or the loads on horizontal cylinders passing through the water-air interface [8,9]. Between water entry and exit, the entry problem has been more heavily studied [10]. Numerous fundamental studies on the water exit of bodies have dealt with symmetric bodies in axisymmetric flows [8,9,11–13]. As there are no available models or experimental data for a lifting body during this transition, researchers have made their own approximations. One proposed solution is a linear scaling factor for the lift generated

^{*}rwaghel@ncsu.edu

[†]Corresponding author; email address: mbryant@ncsu.edu

based on the wetted area of the wing [14]. Under this assumption, as the wing transitions between water and air, the lift is simply assumed to vary linearly from the water to air values. As this assumption has not been directly validated, its applicability has, until now, remained unknown.

A testing apparatus has been constructed to characterize the lift of a wing translating through the water-air interface. In addition to using the data from the experiments for comparison with existing approximations, the effects of angle of attack, velocity, and starting depth are studied. The remainder of the paper is organized as follows. Section II details the experimental setup and procedures. Section III provides comparisons to existing models and the effects of angle of attack, velocity, and starting depth on the lift during egress. A visual comparison of surface deformation during egress is also presented along with a partial explanation for the observed peaks. Section IV provides the conclusions from this paper.

II. METHODS

A. Experimental setup

Experiments are conducted in a 98 000-liter (26 000-gallon) quiescent freshwater reservoir with a depth of 1.83 meters. The filtration system is turned off while testing to minimize external disturbances. A linear motion testing apparatus built using extruded aluminum supports a linear rail as shown in Fig. 1. A ball-bearing linear rail slider provides smooth motion of the wing while traversing below the water and through the water-air surface. To minimize the interaction with the support structure, the load cell and wing mount are mounted on a 0.1 m support sting. The wing is separated 0.06 m from the load cell by a streamlined wing mount. This wing-load cell spacing is consistent with the apparatus used by Mancini *et al.* [15] for an impulsively started wing. Both the support sting and the wing mount feature forward sweep to ensure that the wing is the first component to break the water-air surface. The net distance between the wing and the base plate is 0.16 m or 1.6 chord lengths. The angle of attack on the wing is set using the bolt pattern on the wing mount and a different wing mount is fabricated for each angle of attack setting. As a result, the relevant load cell measurement axis always aligns with the aerodynamic/hydrodynamic lift axis.

An aspect ratio 4 wing with NACA 0015 airfoil section is fabricated using a Stratasys Objet 30 Polyjet 3D printer. This wing has a chord of 0.1 m, features a glossy finish, and is reinforced with two hollow aluminum tubes. The linear rail allows the wing to travel 9.7 chord lengths underwater and approximately 2.5 chords in air.

To achieve constant wing velocity, feedback control is used. The wing is actuated using a brushed DC motor equipped with a US Digital E6 optical encoder. This encoder has a resolution of 3600 counts per revolution, or 0.011mm with the sprockets used in this experiment, and is clocked at 6 MHz. A timing belt and sprocket assembly are used to connect with the wing base plate as shown in Fig. 1. Proportional-integral-derivative (PID) control logic is programed in Simulink, and implemented in real-time using dSpace 1103 Field Programmable Gate Array (FPGA) and ControlDesk Next Generation. The motor is powered using an APS 125 power amplifier. The same dSpace FPGA concomitantly interfaces with the load cell and records data at 1 kHz.

To avoid impulse loading on the load cell and exciting excessive structural vibrations, a two-stage motion control strategy is implemented. In the first stage, the velocity of the wing carriage is gradually increased to the desired velocity as shown in Fig. 2. The velocity increase occurs over a distance of one chord length. In the second stage, constant velocity is maintained throughout the interface transition phase until the test is terminated with the limit switch shown in Fig. 1.

The force sensing for this experiment is achieved through a waterproof (IP-68 rated) ATI Nano25 six-axis load cell. The load cell on the support sting is mounted such that lift is along the load cell's x -measurement axis, which offers superior force resolution (1/48 N) and is unaffected by the depth-dependent hydrostatic forces acting along the z -measurement axis. The force measurements are passed through an accompanying signal conditioner and then recorded by the dSpace FPGA.

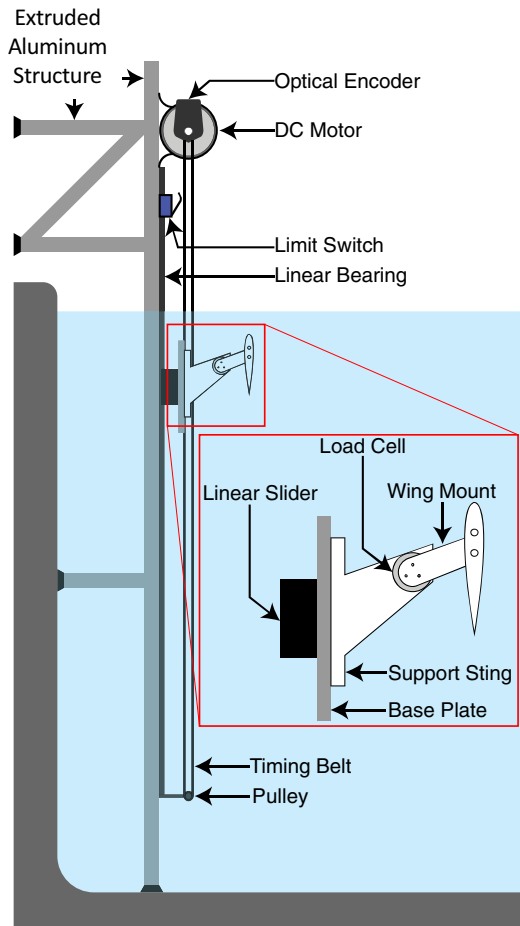


FIG. 1. Schematic of experimental apparatus in testing reservoir. Note: Not to scale.

The water surface deformation during wing egress is visualized with a mixture of oil and rhodamine 6G on the water surface and clear nail polish and rhodamine on the wing. The rhodamine is illuminated by a green laser line located above the wing. The orange fluorescence line is captured using a Photron AX200 monochrome camera with a Wratten No. 21 filter [16] at 500 frames per second with a fixed shutter speed of 1 ms. The frames extracted from video are used to visualize the surface deformation.

B. Procedure

Each trial starts with the wing at the initial depth and angle of attack. A 3-min dwell time is then allowed for large-scale turbulence structures from previous motion to dissipate [17]. During the dwell time, an operator enters the test parameters in the dSpace software interface, CONTROLDESK NEXT GENERATION. When the wing motion is initiated, the wing automatically goes through the velocity increase and the constant velocity stages and crosses the water-air surface. The motion is terminated with the limit switch.

The data presented for each condition in this paper represents the mean of ten identical trials. As this data is collected from an accelerated translating system, vibrations from the structure and drive system are present. The high-frequency noise in the data is attenuated using a fourth-order low-pass

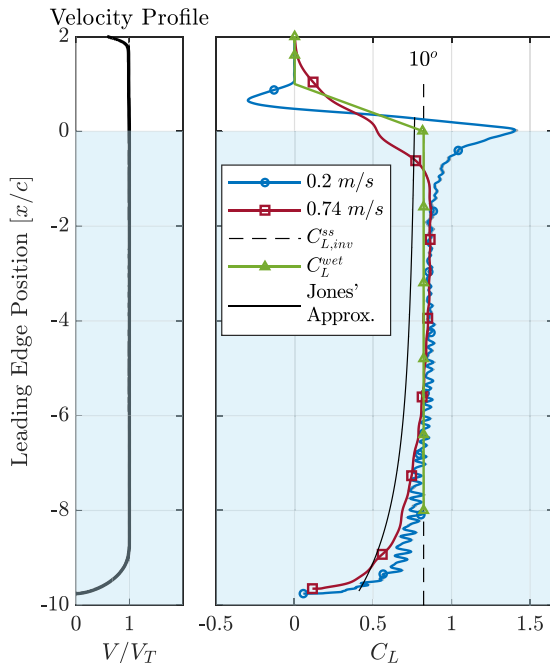


FIG. 2. Left: Measured velocity profile of experimental trials. Right: Comparison of experimental C_L profiles at 10° angle of attack to Jones's impulsively started wing, wetted area scaling, and steady-state approximations.

filter. The filter break frequency is 60 Hz or greater. The low-pass cutoff frequency was chosen to illustrate the presence of vibrations, while at the same time not oversmoothing the load peaks at the interface transition. By using forward and backward filtering, the phase distortion is minimized. To capture the variation of the experimental data, grey regions are used in all plots to mark one standard deviation above and below the mean value.

III. RESULTS AND DISCUSSION

The coefficient of lift, C_L , for a finite wing in steady state, either in air or water, is defined as

$$\text{Air : } C_L^a = \frac{L}{\frac{1}{2}\rho_a V^2 S}, \quad (1)$$

$$\text{Water : } C_L^w = \frac{L}{\frac{1}{2}\rho_w V^2 S}, \quad (2)$$

where L is lift force, ρ_w is density of water, ρ_a is density of air, V is the wing velocity, and S is the wing planform area. When the wing transitions from water to air, the standard definitions of density and wing planform area become invalid.

Figure 2 shows the experimentally determined lift coefficient and velocity profile of the wing undergoing water to air egress. In this case, the wing leading edge starts at approximately 9.7 chord lengths below the water surface and breaks the nominal surface at zero position. The coefficient of lift for all experimental runs in this paper is calculated using Eq. (2); this nondimensionalization allows consistent comparison and also attenuates noise when the wing is in air.

The inviscid steady-state coefficient of lift, $C_{L,inv}^{ss}$ in Fig. 2 is calculated using Prandtl's lifting-line theory (LLT). The airfoil lift-curve slope value of 0.12° for the NACA 0015 airfoil is calculated

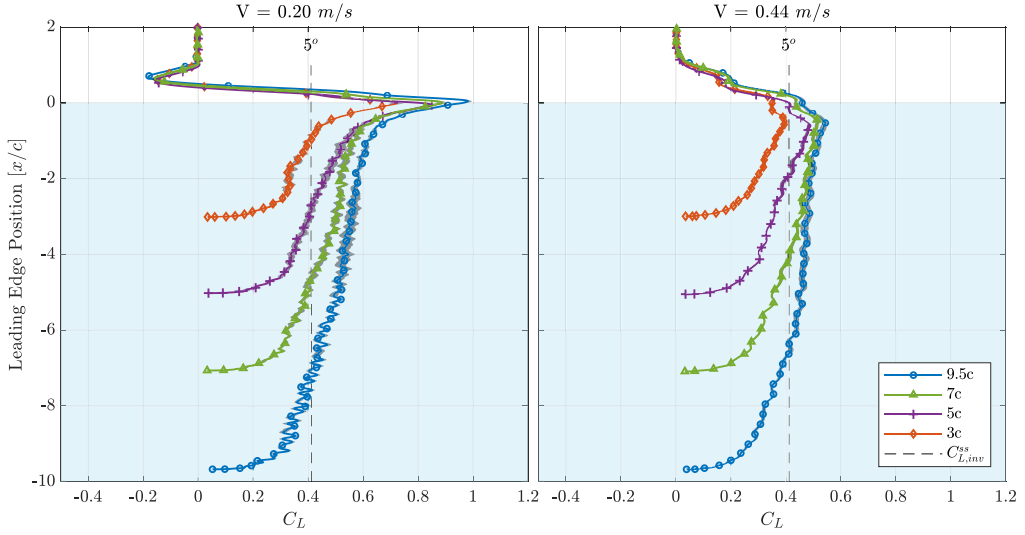


FIG. 3. The coefficients of lift versus leading edge position at 0.2 m/s and 0.44 m/s with starting depths of 9.7, 7, 5, and 3 chords at 5° angle of attack.

for inviscid flow using XFOIL [18]. The steady-state wing lift coefficient is calculated using Eq. (3).

$$C_{L,inv}^{ss} = C_{l_\alpha} \frac{AR}{AR + 2} \alpha \quad (3)$$

where $C_{L,inv}^{ss}$ is the inviscid steady-state lift coefficient, C_{l_α} is the inviscid airfoil lift curve slope from Xfoil, AR is the wing aspect ratio, and α is the angle of attack. This inviscid approximation is shown in lieu of other models for wing lift at low Reynolds numbers to provide a simple baseline of comparison for the egress phenomenon and to illustrate whether or not viscous effects are significant in the submerged lift generation of the wing for each test case. Moreover, Tank *et al.* [19] show that agreement among experiments and computational methods is difficult to achieve at low Reynolds numbers. The experimental steady-state submerged lift in Fig. 2 exhibits good agreement with the inviscid model, indicating that viscous effects are not significant for these conditions. Other conditions tested (cf. Fig. 3) show stronger low Reynolds number effects in the submerged lift generation. The $C_{L,inv}^{ss}$ is provided throughout to highlight these differences. It is not intended or purported to account for the complex flow conditions that occur at low Reynolds number conditions.

When the wing reaches steady-state velocity, the measured C_L does not instantaneously approach the $C_{L,inv}^{ss}$ approximated using inviscid methods. This phenomenon is well documented in literature and was first observed by Wagner [20]. Jones's approximation provides an algebraic model for wing lift for an impulsively started wing prior to reaching steady state [21]:

$$C_L = C_{l_\alpha} \alpha \phi \frac{AR}{AR + 2}, \quad \text{where} \quad (4)$$

$$\phi = 1 - 0.165e^{-0.0455s} - 0.335e^{-0.3s},$$

where C_{l_α} is the airfoil lift-curve slope, $\partial C_l / \partial \alpha$, α is angle of attack, ϕ is an experimental parameter, AR is the aspect ratio, and s is the distance traveled in semichords. These early works used an impulsive start and showed that the C_L typically starts at half the steady-state value. The experiment in this paper used a different velocity profile but the previous observations help explain the increase in C_L as the wing moves forward and compares closely with Jones's approximation plotted in Fig. 2

for impulsively started wings. In this experiment, the wing approaches steady state several chords prior to egress and, as a result, the variations in lift during egress are deemed not related to the initial start of the wing but caused by the water-air surface interacting with the wing. Thus, we can proceed to investigate the effects of egress separately.

As the wing approaches the surface, the lift starts to deviate from the asymptotically approached steady-state C_L . In the slower case with an egress velocity of 0.2 m/s, there is a sharp increase in the C_L starting around one chord below the surface whereas in the faster case with an egress velocity of 0.74 m/s, the wing experiences a loss of lift around this same depth. Due to these observations, egress effects are considered to start near one chord depth. This velocity-dependent C_L behavior has not been previously studied in literature and motivates further investigation.

As the wing egresses from the water to air, the experimentally measured lift is highly repeatable. Intuitively, this portion of the data would be rife with noise and variability. The grey regions in Fig. 2 are difficult to see for most of the lift profile but are particularly narrow during the egress. This observation applies not only to Fig. 2 but to all cases presented in this paper and provides the basis that a phenomenological model can be developed.

During the egress, the wing is partially under water and partially in air. As a result, the definition of C_L in Eq. (2) becomes invalid. One approach for modeling a wing undergoing water to air egress proposed by Siddall and Kovac [14] used wetted area scaling, i.e., the total lift is the sum of contributions from the area of the wing under the water and the area in air,

$$L = \frac{1}{2}\rho_w V^2 C_L A_{\text{wet}} + \frac{1}{2}\rho_a V^2 C_L (S - A_{\text{wet}}) \quad (5)$$

where A_{wet} is the wetted planform area of the wing area under the nominal water surface. This simple model for lift during egress assumes that C_L remains constant and that the lift scales with the wetted area and dynamic pressure of each fluid medium. This formulation can be more succinctly described in Eq. (6):

$$L = \frac{1}{2}\rho_a V^2 C_L S Q, \quad (6)$$

where Q is the scaling factor defined in Eq. (7) [14].

$$Q = \left(\frac{\rho_w}{\rho_a} \frac{A_{\text{wet}}}{A_{\text{total}}} + \left(1 - \frac{A_{\text{wet}}}{A_{\text{total}}} \right) \right). \quad (7)$$

This approximation readily calculates the lift force but the comparison in Fig. 2 requires a coefficient. For this comparison, an equivalent wetted area scaled lift coefficient, C_L^{wet} , is defined in Eq. (8).

$$C_L^{\text{wet}} = \frac{\rho_a}{\rho_w} C_L Q \quad (8)$$

This equivalent lift coefficient is plotted in Fig. 2. As this approximation is egress velocity independent, it fails to capture the variation in lift before and during egress. To develop a more complete understanding of lift during egress, the effects of starting depth, velocity, and angle of attack are experimentally studied in this paper.

A. Effect of starting depth

To confirm that the egress C_L profiles observed in Fig. 2 are due to egress and not starting depth effects; we first investigate the effect of the initial wing proximity to the free-surface to eliminate this potential variability from further results. The implications of starting depth on the egress lift profile is investigated at $\alpha = 5^\circ$ for $V = 0.2$ m/s and $V = 0.44$ m/s by starting experiments at depths of 9.7, 7, 5, and 3 chords below the surface. These experiments are used to compare effects of starting depth on the egress lift profile (Fig. 3) and lift development (Fig. 4).

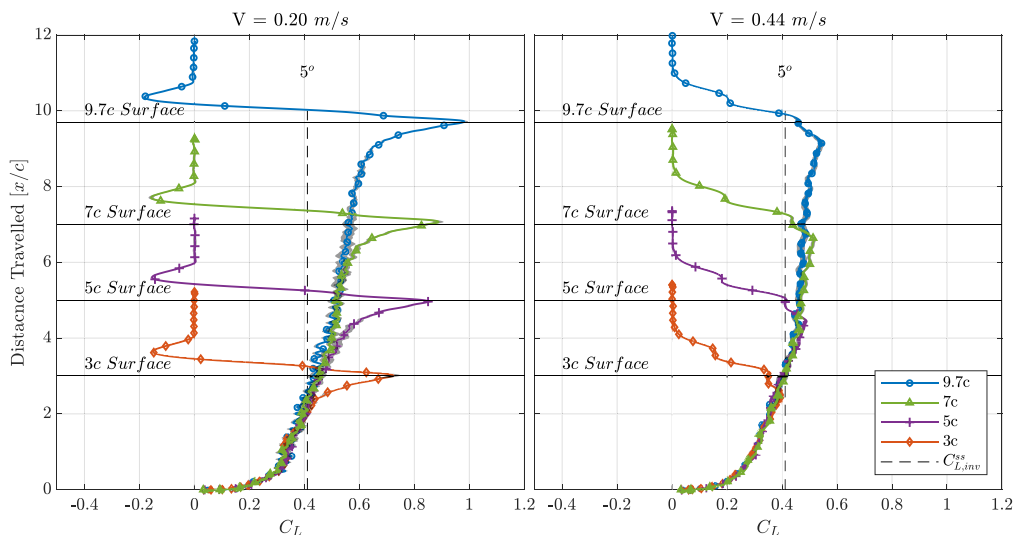


FIG. 4. The coefficients of lift versus distance traveled at $V = 0.2$ m/s and $V = 0.44$ m/s with starting depths of 9.7c, 7c, 5c, and 3c at 5° angle of attack.

The egress lift profile is qualitatively compared by plotting leading edge position versus C_L in Fig. 3. It appears that while the C_L egress profiles scale slightly with depth, the overall shape remains similar. For all of the test cases presented in this paper, an initial C_L growth is observed. This growth toward a steady-state value is typical with impulsively started wings as predicted by Wagner's method. The deeper the starting depth, the larger the peak value reached during the trial, C_L^p . For the $V = 0.2$ m/s test case, the negative peak, C_L^{np} , showed much lower sensitivity to starting depth than the positive peak. For the $V = 0.44$ m/s test case, the overall profile seems to be evenly scaled with starting depth. For both the 0.2 m/s and 0.44 m/s tests, as the starting depth increased, the sensitivity to starting depth decreased.

To determine if differences in C_L values were primarily due to egress effects specific to the starting depth or the continued lift development predicted by Jones's approximation, the lift profiles are compared by plotting distance traveled versus C_L . This comparison reveals that prior to egress effects, the C_L profile is independent of starting depth, as shown in Fig. 4. The C_L profiles for the 3-, 5-, and 7-chord starting-depth test cases overlap the 9.7 chord starting-depth test case until they diverge prior to egress. This trend implies that the initial lift increase is insensitive to starting depth to approximately one chord depth. For the 0.20 m/s case, the location of divergence is approximately one chord below the surface for the 9.7-, 7-, and 5-chord starting-depth cases and approximately 0.75 chords for the 3-chord starting-depth test case. In the 0.2 m/s egress, the positive peak scales with the higher C_L of the deeper starting-depth cases, however, the negative peaks remain unaffected. Because the $V = 0.44$ m/s profiles do not show a pronounced peak in C_L prior to the leading-edge reaching the surface, only the 0.2 m/s case is quantitatively evaluated. As egress effects appear to start around a depth of one chord, except for the three-chord starting-depth case, the C_L from this depth is used as a point of comparison and is given as C_L^1 . While it is expected that the lift might continue to change if the water surface were not present, for this paper the comparison is made to C_L^1 to focus on the effects of the transition. The relative magnitude of C_L^p/C_L^1 shows low sensitivity to starting depth, as it is approximately 60% for all starting depths. The C_L profiles for the 3-, 5-, and 7-chord starting-depth cases overlap the 9.7-chord starting-depth case prior to divergence, which shows that the egress lift profiles are not caused by the starting depth. Based on these results, all subsequent experiments use a fixed starting depth of 9.7 chords.

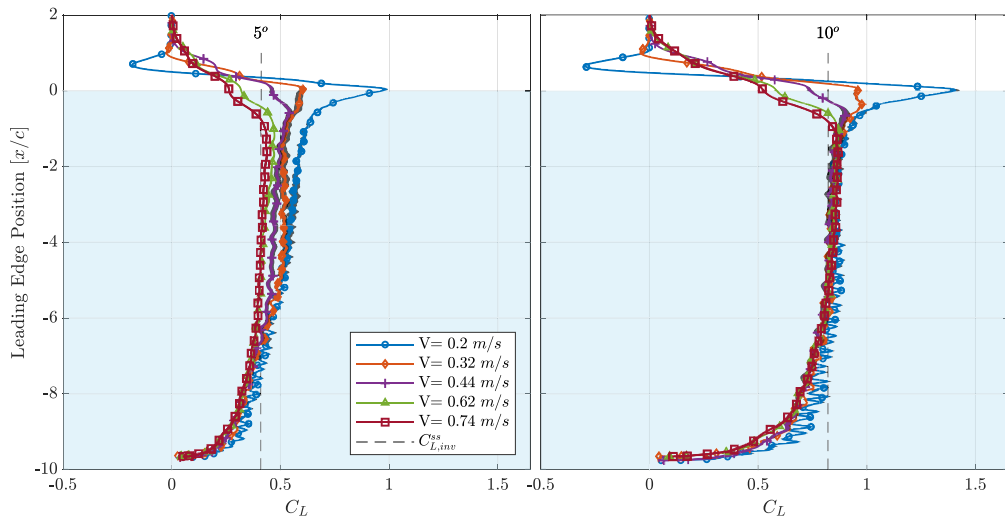


FIG. 5. The coefficients of lift at 0.2, 0.32, 0.44, 0.62, and 0.74 m/s at 5° and 10° angle of attack.

B. Effect of velocity

To observe the effects of velocity on lift, experiments are conducted at 0.2 m/s, 0.32 m/s, 0.44 m/s, 0.62 m/s, and 0.74 m/s at both 5° and 10° angles of attack. The vehicle presented by Weisler *et al.* [5], has an egress velocity of three to four chords per second, which is included in the testing range considered here of two to seven chords per second. Results from these tests are shown in Fig. 5 and provide strong evidence that lift during egress is dependent on velocity. For both the 5° and 10° cases, the maximum C_L value and its location change with velocity. In the 0.2 m/s case, the peaks occur when the wing leading edge breaks the water surface. However, as the velocity increases, the magnitude of the peaks decrease. This trend continues until, for the 0.74 m/s case, there is no peak but rather just a decrease in lift. The magnitude of C_L at each peak is written as C_L^p . In addition, the location of the peak or decrease point increases from 0-chord depth to approximately 1.2 chords depth for the 0.2 m/s and 0.74 m/s cases, respectively. Table I shows that as velocity increases, C_L decreases when the wing begins to break the surface, C_L^0 . For example, with $\alpha = 5^\circ$ and the leading edge at $x/c = 0$, $C_L^0 = 0.97$ for $V = 0.2$ m/s case, whereas $C_L^0 = 0.26$ for $V = 0.74$ m/s case. Thus, as the leading edge breaks the surface for the slowest case at 5° , the C_L is nearly four times greater than that for the fastest test case. However, this same comparison for the 10° case reveals that the C_L is only three times greater for the slowest case than the fastest case. This demonstrates that the egress is sensitive to velocity and also angle of attack. It is observed that for the 10° case, the C_L profile prior to egress is similar for all velocities. However, for the 5° case, before the egress effects begin, the C_L profile shows continued growth beyond LLT, especially for slower test cases. As these tests are conducted over a range of Reynolds numbers from 20 000 to 80 000, the discrepancies in the

TABLE I. C_L^p , C_L^p/C_L^1 , and C_L^0 for 0.2, 0.32, 0.44, 0.62, and 0.74 m/s at 5° and 10° angles of attack. Note the decreasing trends with increasing velocities.

α	5°					10°				
Velocity [m/s]	0.2	0.32	0.44	0.62	0.74	0.2	0.32	0.44	0.62	0.74
C_L^p	0.98	0.60	0.54	0.47	0.44	1.40	0.98	0.90	0.87	0.86
C_L^p/C_L^1 [%]	160	110	100	100	100	150	110	100	100	100
C_L^0	0.97	0.60	0.46	0.32	0.26	1.40	0.96	0.74	0.59	0.53

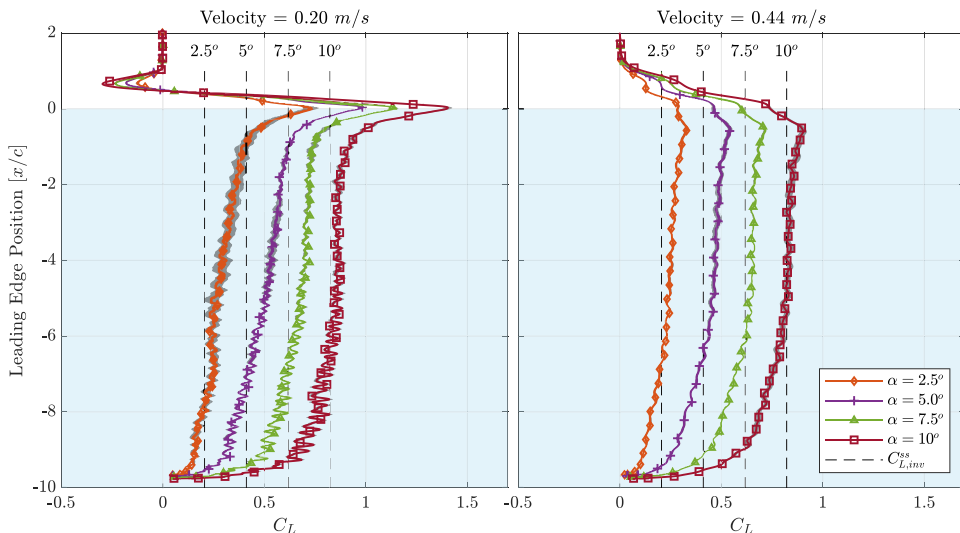


FIG. 6. The coefficients of lift at $\alpha = 2.5^\circ$, 5° , 7.5° , and 10° at 0.20 m/s and 0.44 m/s.

5° case are possibly due to flow transition effects and laminar separation bubbles at these relatively low Reynolds numbers [22]. Work by Mancini *et al.* [23] presents experimental results showing that for an impulsively started wing at low Reynolds numbers, the C_L for these angles of attack may still be well above $C_{L,inv}^{ss}$ even after travel of 14 chords. As this present paper is focused on the lift changes during the water to air egress and not on the flow development at low Reynolds numbers of impulsively started wings, these results are still useful for showing the egress trends. Additionally, the results help demonstrate that these transition effects occur with or without the presence of Re number effects. The dominant factor that appears to determine when and if the lift spikes occur is velocity.

C. Effect of angle of attack

The effect of angle of attack is evaluated at 2.5° , 5° , 7.5° , and 10° at wing translation speeds of 0.2 m/s and 0.44 m/s. The resulting C_L profiles are shown in Fig. 6. Figure 6 shows that angle of attack scales C_L across the entire time history for both velocities with higher angles of attack resulting in higher C_L values. However, when evaluating the C_L values for the 0.2 m/s case, an interesting dependence of the maximum C_L on angle of attack is observed. At this speed, a large peak in C_L is noted. Increasing the angle of attack not only increases the steady C_L values but also increases the C_L^p . The relative size of the peak is observed by calculating the ratio of C_L^p to C_L^1 . For example, the 2.5° case at 0.20 m/s has a $C_L^p/C_L^1 = 180\%$ while for the 10° case it is 150% . This same trend of decreasing relative contributions of egress effects to C_L^1 is not clearly observed in the 0.44 m/s case. For the 0.44 m/s case, C_L^p/C_L^1 were 110% and 100% for 2.5° and 10° , respectively.

For both cases, the C_L values begin to experience egress effects when the wing's leading edge is approximately one chord from the water surface. For the 0.2 m/s case, the C_L value begins to grow while, for the 0.44 m/s case, C_L initially grows but then starts to decrease. For the 0.2 m/s case, the negative peaks, C_L^{np} , appear to be slightly sensitive to angle of attack, decreasing from -0.13 to -0.30 for 2.5° and 10° , respectively. However, when compared to C_L^1 , the negative peaks appear to be insensitive with a constant value of approximately $30\% C_L^1$. Comparing C_L^p to C_L^1 shows a decreasing trend with increasing angle of attack, going from 180% to 150% for 2.5° and 10° , respectively. Interestingly, the relative size of the positive peak to C_L^1 decreases with increasing angle of attack, while the negative peak is unchanged.

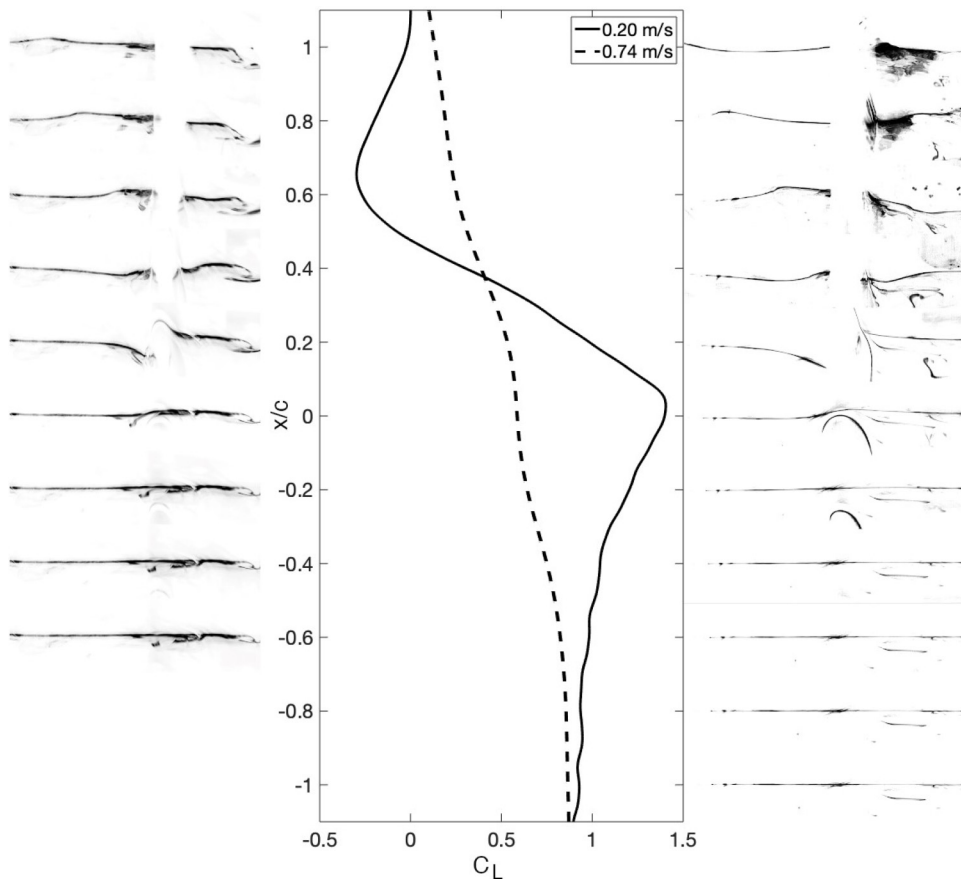


FIG. 7. Image composite of water-surface deformation during wing egress for $V = 0.74$ m/s [27] (left) and $V = 0.2$ m/s [28] (right) at $\alpha = 10^\circ$ and corresponding lift coefficient. Each image corresponds to the position of the leading edge of the wing with respect to the surface. The wing is rotated 10° CCW in the images.

D. Surface deformation comparison

The deformation of the water surface when the wing egresses out of water is visually compared for the $V = 0.2$ m/s and $V = 0.74$ m/s cases at $\alpha = 10^\circ$. The wing is oriented with a 10° rotation counterclockwise, producing a lift force to the left in the images. The comparisons are made by extracting select frames from videos of the egresses as shown in Fig. 7. The image of the surface is placed at the corresponding position of the wing's leading edge in the center plot, so as to directly compare the surface deformation to the measured wing lift coefficient. One can easily observe that the surface is completely flat when the leading edge is at $x/c = -0.2$, and only a small surface disturbance is visible at $x/c = 0$ for the lower motion velocity of $V = 0.2$ m/s. As the wing transitions through the interface, the surface is lowered on the suction side (left), and waves eventually emanate out to both left and right sides from the wing.

E. Fluid energy explanation for lift peak

To determine if there is an analytical explanation for the deviation from the wetted area-scaling observed in the transition region $-1 < x/c < 0$, the forces were evaluated from the basis of fluid kinetic energy, which has an inviscid assumption. Brennen [24] provide a thorough review of the subject. The observed presence of a peak in lift can be partially explained by evaluating the

specific force per volume, F for the motion of a rigid body in a general direction. In unbounded incompressible flow, the integral in Eq. (9) is an invariant I (a volume) of all relative velocity out to infinity:

$$F = \frac{-1}{U} \frac{dT}{dt} = \frac{-1}{U} \frac{d}{dt} \left(\frac{\rho U^2}{2} \int \frac{u_i}{U} \frac{u_i}{U} dV \right) = \frac{-\rho}{2U} \frac{d}{dt} \left(U^2 \int \frac{u_i}{U} \frac{u_i}{U} dV \right) = \frac{-\rho}{2U} \frac{d}{dt} (U^2 * I). \quad (9)$$

For a motion in the presence of a surface, with x upward, the integral is now dependent on the distance to the surface since the relative velocity of the surrounding fluid u_i/U changes with proximity to the surface and is thus given as $I(x)$. Denoting the force in the direction of the motion as drag D and substituting the invariant integral in Eq. (9) with $I(x)$ to account for this proximity effect yields

$$D = \frac{-\rho}{2U} \frac{d}{dt} (U^2 * I(x)) = \frac{-\rho}{2U} 2U \frac{dU}{dt} * I(x) - \frac{\rho}{2U} U^2 \frac{dI(x)}{dx} \frac{dx}{dt} = -\rho I(x) \frac{dU}{dt} - \frac{\rho U^2}{2} \frac{dI(x)}{dx}. \quad (10)$$

The first term, $-\rho I(x)$, is known as the regular apparent mass, which results in an additional drag force when accelerating a body with dU/dt , if $I(x)$ is constant and not dependent on any position x . For constant velocity motion, the specific drag force is now shown to only be dependent on how $I(x)$ changes with distance to a boundary of another body or the surface. Greenhow and Yanbao [25] demonstrated how the integral varies for a cylinder translating in the normal direction to the surface with a velocity U , providing a force away from the surface, irrespective of the direction of the motion. If the additional drag force is normalized with this velocity U and the wing planform area S , we obtain

$$C_D = \frac{D}{\frac{1}{2} \rho U^2 S} = \frac{-\frac{\rho U^2}{2} \frac{dI(x)}{dx}}{\frac{1}{2} \rho U^2 S} = \frac{-1}{S} \frac{dI(x)}{dx}. \quad (11)$$

Such analysis has yet to be derived for a lifting body, but we acknowledge from Brennen's work [24] that the apparent mass is actually a symmetric matrix I_{ij} , which can produce forces (and moments) in other directions than a rectilinear motion. An example of this was done by Granlund *et al.* [26], who treated an airfoil at an angle-of-attack as a thin ellipse with a rotated coordinate system, experiencing both lift and drag from a kinetic energy change in the streamwise direction.

From this knowledge, we expect the lift coefficient in this paper to change with proximity to the surface as $I(x)$ must increase as we near the surface. It can be shown for a cylinder that the $dI_{11}(x)/dx$ is a positive finite value when touching the surface, so therefore it is a peak [25]. The lack of deformation in the surface visualization prior to the wing breaking the surface, as shown in Fig. 7, also supports that the interface should be treated as a solid boundary. The presence of a peak is consistent with the results reported in this paper for some cases. However, Eq. (11) is not dependent on velocity, which contradicts the experimental results. Since the derivation assumes that the invariant is only dependent on the interface proximity, we conclude that for a lifting body with circulation, it must also implicitly be dependent on the velocity, albeit to a yet unknown relationship. This relationship will be further explored and reported in future scientific publications.

IV. CONCLUSIONS

This paper presents an experimental investigation of the effects of angle of attack, velocity, and starting depth on wing lift when egressing from water to air. A 0.1-m chord NACA 0015 wing with an aspect ratio of 4 is used for the experiments. Lift is measured using a waterproof load cell and nondimensionalized lift histories are calculated for each test case. The results show that although C_L increases throughout the motion for increasing angle of attack, the ratio of C_L^p to C_L^l decreases with increasing angle of attack. At some conditions, a rapid increase in lift during egress is observed growing nearly 1.8 times over one chord of travel. The velocity of the egress has a very strong effect

on the C_L profile observed. At the slowest test velocities, a large positive spike in lift occurs when the leading edge breaks the surface. However, before the wing completely exits the water, a negative spike in lift is observed. As egress velocity increases, the maximum C_L decreases, the depth of the maximum moves from the water surface to around 1.2 chords below the surface, and the egress profile becomes increasingly linear. It is observed that the starting depth did not affect the shape of the egress lift profile, but did affect the relative magnitude of the peak value. This effect on the peak value is caused by continued flow development while the wing is submerged.

The assumption that the C_L profile during egress is solely dependent on the wetted area of the wing is evaluated. While the faster egresses exhibit a more linear lift decrease than the slower cases, the lift is observed to start changing well below the free mean water surface. Furthermore, the slower cases exhibit a large spike in lift as the wing breaks the water surface. These discrepancies demonstrate that a simple wetted area scaling method is not sufficient to model the lift generation of a wing during this egress as velocity dependencies cannot be accounted for. The observed spike in lift was partially attributed to the change in surrounding fluid kinetic energy due to the air-water interface. As the experiments revealed a dependence on both position and velocity for the spikes in lift, additional work is needed to determine an accurate explanation.

As design of fixed-wing vehicles capable of transitioning from water to air continues, additional work is needed to model and better understand the underlying physics during egress. Our experiments demonstrate that the lift generation of an egressing wing is highly sensitive to velocity and can even include lift direction reversals during the egress. Thus, depending on the velocity of cross-domain unmanned vehicles, widely varying forces during egress could be encountered. To successfully perform egresses in varying conditions, the vehicle control systems will need to be able to account for these complex and variable egress lift behaviors.

ACKNOWLEDGMENTS

The authors acknowledge help from M. Bonds with producing the surface visualizations.

-
- [1] Y. Chen, E. F. Helbling, N. Gravish, K. Ma, and R. J. Wood, Hybrid aerial and aquatic locomotion in an at-scale robotic insect, in *Proceedings of the IEEE International Conference on Intelligent Robots and Systems*, (IEEE, Piscataway, 2015), p. 331.
 - [2] M. M. Maia, P. Soni, and F. J. Diez-Garcias, Demonstration of an aerial and submersible vehicle capable of flight and underwater navigation with seamless air-water transition, in *Proceedings of Xponential 2016—An AUVSI Experience* (AUVSI, Los Angeles, California, 2016).
 - [3] R. Siddall, A. Ortega Ancel, and M. Kovač, Wind and water tunnel testing of a morphing aquatic micro air vehicle, *Interface Focus* **7**, 20160085 (2017).
 - [4] W. Stewart, W. Weisler, M. Macleod, T. Powers, A. Defreitas, and R. Gritter, Design and demonstration of a seabird-inspired fixed-wing hybrid UAV-UUV system, *Bioinspiration & Biomimetics* **13**, 056013 (2018).
 - [5] W. Weisler, W. Stewart, M. B. Anderson, K. J. Peters, A. Gopalarathnam, and M. Bryant, Testing and characterization of a fixed wing cross-domain unmanned vehicle operating in aerial and underwater environments, *IEEE J. Oceanic Eng.* **43**, 969 (2017).
 - [6] Y. H. Tan, R. Siddall, and M. Kovac, Efficient aerial-aquatic locomotion with a single propulsion system, *IEEE Robotics Automation Lett.* **2**, 1304 (2017).
 - [7] W. Stewart, W. Weisler, M. Anderson, M. Bryant, and K. Peters, Dynamic modeling of passively draining structures for aerial-aquatic unmanned vehicles, *IEEE J. Oceanic Eng.* **45**, 840 (2019).
 - [8] M. Greenhow, Water-entry and-exit of a horizontal circular cylinder, *Appl. Ocean Res.* **10**, 191 (1988).
 - [9] B. Y. Ni, A. M. Zhang, and G. X. Wu, Simulation of complete water exit of a fully-submerged body, *J. Fluids Structures* **58**, 79 (2015).

-
- [10] R. Rajavaheinthan and M. Greenhow, Constant acceleration exit of two-dimensional free-surface-piercing bodies, *Appl. Ocean Res.* **50**, 30 (2015).
- [11] S. K. Chow, A. Y. Hou, and L. Landweber, Hydrodynamic forces and moments acting on a body emerging from an infinite plane, *Phys. Fluids* **19**, 1439 (1976).
- [12] A. A. Korobkin, A linearized model of water exit, *J. Fluid Mech.* **737**, 368 (2013).
- [13] B. Y. Ni and G. X. Wu, Numerical simulation of water exit of an initially fully submerged buoyant spheroid in an axisymmetric flow, *Fluid Dyn. Res.* **49**, 045511 (2017).
- [14] R. Siddall and M. Kovac, Fast aquatic escape with a jet thruster, *IEEE/ASME Trans. Mechatronics* **22**, 217 (2017).
- [15] P. Mancini, F. Manar, K. Granlund, M. V. Ol, and A. R. Jones, Unsteady aerodynamic characteristics of a translating rigid wing at low Reynolds number, *Phys. Fluids* **27**, 123102 (2015).
- [16] K. O. Granlund, M. V. Ol, and L. P. Bernal, Unsteady pitching flat plates, *J. Fluid Mech.* **733**, R5 (2013).
- [17] A. R. Jones and H. Babinsky, Reynolds number effects on leading edge vortex development on a waving wing, *Exp. Fluids* **51**, 197 (2011).
- [18] M. Drela, XFOil 6.99, <https://web.mit.edu/drela/Public/web/xfoil/> (2013).
- [19] J. Tank, L. Smith, and G. R. Spedding, On the possibility (or lack thereof) of agreement between experiment and computation of flows over wings at moderate Reynolds number, *Interface Focus* **7**, 20160076 (2017).
- [20] H. Wagner, Über die Entstehung des dynamischen Auftriebes von Tragflügeln, *Z. Angew. Math. Mech.* **5**, 17 (1925).
- [21] R. Jones, The unsteady lift of a wing of finite aspect ratio, Technical Report No. NACA NACA-TR-681 NASA Technical Reports Server, 1940.
- [22] E. V. Laitone, Wind tunnel tests of wings at Reynolds numbers below 70 000, *Exp. Fluids* **23**, 405 (1997).
- [23] P. M. Mancini, A. R. Jones, K. O. Granlund, and M. V. Ol, Unsteady aerodynamic response of a rapidly started flexible wing, *Int. J. Micro Air Vehicles* **7**, 147 (2015).
- [24] C. E. Brennen, A review of added mass and fluid inertial forces, Technical Report No. CR 82.010, Naval Civil Engineering Laboratory, Port Hueneme, CA (1982).
- [25] M. Greenhow and L. Yanbao, Added masses for circular cylinders near or penetrating fluid boundaries—review, extension and application to water-entry, -exit and slamming, *Ocean Eng.* **14**, 325 (1987).
- [26] K. Granlund, B. Monnier, M. Ol, and D. Williams, Airfoil longitudinal gust response in separated vs. attached flows, *Phys. Fluids* **26**, 027103 (2014).
- [27] See Supplemental Material at <https://link.aps.org/supplemental/10.1103/PhysRevFluids.6.054002> for a video of the 0.74 m/s motion.
- [28] See Supplemental Material at <https://link.aps.org/supplemental/10.1103/PhysRevFluids.6.054002> for a video of the 0.20 m/s motion.